

# Characterization and Surface Reactivity of Ferrihydrite Nanoparticles Assembled in Ferritin

Gang Liu,<sup>†</sup> Sudeep Debnath,<sup>†</sup> Kristian W. Paul,<sup>‡</sup> Weiqiang Han,<sup>§</sup> Douglas B. Hausner,<sup>†</sup> Hazel-Ann Hosein,<sup>†</sup> F. Marc Michel,<sup>||</sup> John B. Parise,<sup>||</sup> Donald L. Sparks,<sup>‡</sup> and Daniel R. Strongin<sup>\*,†,||</sup>

Department of Chemistry, Temple University, 1901 North 13th Street, Philadelphia, Pennsylvania 19122, Department of Plant and Soil Sciences, University of Delaware, Newark, Delaware 19716, Center for Functional Nanomaterials, Brookhaven National Laboratory, Upton, New York 11973, and Center for Environmental Molecular Science, The State University of New York at Stony Brook, Stony Brook, New York 11794

Received January 23, 2006. In Final Form: August 21, 2006

Ferrihydrite nanoparticles with nominal sizes of 3 and 6 nm were assembled within ferritin, an iron storage protein. The crystallinity and structure of the nanoparticles (after removal of the protein shell) were evaluated by high-resolution transmission electron microscopy (HRTEM), atomic force microscopy (AFM), and scanning tunneling microscopy (STM). HRTEM showed that amorphous and crystalline nanoparticles were copresent, and the degree of crystallinity improved with increasing size of the particles. The dominant phase of the crystalline nanoparticles was ferrihydrite. Morphology and electronic structure of the nanoparticles were characterized by AFM and STM. Scanning tunneling spectroscopy (STS) measurements suggested that the band gap associated with the 6 nm particles was larger than the band gap associated with the 3 nm particles. Interaction of SO<sub>2</sub>(g) with the nanoparticles was investigated by attenuated total reflectance Fourier transform infrared (ATR-FTIR) spectroscopy, and results were interpreted with the aid of molecular orbital/density functional theory (MO/DFT) frequency calculations. Reaction of SO<sub>2</sub>(g) with the nanoparticles resulted primarily in SO<sub>3</sub><sup>2-</sup> surface species. The concentration of SO<sub>3</sub><sup>2-</sup> appeared to be dependent on the ferrihydrite particle size (or differences in structural properties).

## 1. Introduction

In recent years, nanomaterials have received much attention due to their unique size- and crystallinity-dependent optical, electronic, magnetic, and chemical properties.<sup>1</sup> Nanomaterials possess physical and chemical properties that may benefit electronic device development,<sup>2</sup> medicine,<sup>3</sup> catalysis,<sup>4</sup> and environmental remediation.<sup>5–7</sup> A significant amount of research has focused on understanding the structural properties of nanoparticles that lead to their unique reactivity. The reactivity of a nano- versus macrosized material may be dramatically different. In catalysis, the prototypical example is gold.<sup>8</sup> Gold not only has interesting optical properties at the nanoscale, but it also exhibits markedly different reactivity. Nanogold supported on titania catalyzes the oxidation of CO by O<sub>2</sub>, while at larger sizes it is inactive toward this reaction.<sup>9</sup> There is also increasing

awareness that nanoparticles are naturally present in the environment and influence atmospheric<sup>10</sup> and soil chemistry.<sup>11</sup> In the environment, ferrihydrite is an ubiquitous material in aquatic systems and soils<sup>12</sup> and exhibits unique reactivity at the nanoscale.<sup>13</sup> For example, ferrihydrite nanoparticles exhibit a size-dependent ability to oxidize hydroquinone.<sup>13</sup> Other iron oxide nanoparticles found in the environment exhibit size-dependent behavior, such as the role of hematite in the catalytic oxidation of Mn<sup>2+</sup>(aq).<sup>14</sup>

In this investigation, the size-dependent reactivity of ferrihydrite toward the environmentally important gas sulfur dioxide [SO<sub>2</sub>(g)] was studied. SO<sub>2</sub>(g) is frequently generated during the burning of fossil fuels in factories and power plants or is derived from natural processes such as volcanic eruptions. Atmospheric emission of SO<sub>2</sub>(g) affects the environment because it promotes the production of acid rain.<sup>15</sup> Both natural and engineered metal oxides have been utilized as catalysts or sorbents for removal or minimization of SO<sub>2</sub>(g) emissions.<sup>16</sup> Previous studies examined the interaction of SO<sub>2</sub>(g) with various phases and sizes of synthetic iron hydroxides.<sup>17,18</sup> Matsumoto and Kaneko<sup>17</sup> reported for  $\gamma$ -FeOOH nanoparticles in the range of 7–17 nm that SO<sub>2</sub>(g) adsorption led to formation of SO<sub>3</sub><sup>2-</sup> and SO<sub>4</sub><sup>2-</sup> species, and the amount of SO<sub>2</sub>(g) adsorption increased slightly with increasing

\* To whom correspondence should be addressed: phone (215) 204-7199; fax (215) 204-1532; e-mail dstrongi@temple.edu.

<sup>†</sup> Temple University.

<sup>‡</sup> University of Delaware.

<sup>§</sup> Brookhaven National Laboratory.

<sup>||</sup> The State University of New York at Stony Brook.

(1) Burda, C.; Chen, X.; Narayanan, R.; El-Sayed, M. A. *Chem. Rev.* **2005**, *105*, 1025.

(2) Shenhar, R.; Rotello, V. M. *Acc. Chem. Res.* **2003**, *36*, 549.

(3) Parak, W. J.; Gerion, D.; Pellegrino, T.; Zanchet, D.; Micheel, C.; Williams, S. C.; Boudreau, R.; Le Gros, M. A.; Larabell, C. A.; Alivisatos, A. P. *Nanotechnology* **2003**, *14*, R15.

(4) Somorjai, G. A.; Rioux, R. M. *Catal. Today* **2005**, *100*, 201.

(5) Ranjit, K. T.; Medine, G.; Jeevanandam, P.; Martyanov, I. N.; Klabunde, K. J. *Environ. Catal.* **2005**, *391*.

(6) Xu, J.; Bhattacharyya, D. *Environ. Prog.* **2005**, *24*, 358.

(7) Sun, Y.-P.; Li, X.-Q.; Cao, J.; Zhang, W.-X.; Wang, H. P. *Adv. Colloid Interface Sci.* **2006**, *120*, 47.

(8) Meyer, R.; Lemire, C.; Shaikhutdinov, S. K.; Freund, H.-J. *Gold Bull.* **2004**, *37*, 72.

(9) Chen, M. S.; Goodman, D. W. *Catal. Today* **2006**, *111*, 22.

(10) Biswas, P.; Wu, C. Y. *J. Air Waste Manage. Assoc.* **2005**, *55*, 708.

(11) Waychunas, G. A.; Kim, C. S.; Banfield, J. F. *J. Nanopart. Res.* **2005**, *7*, 409.

(12) Jambor, J. L.; Dutrizac, J. E. *Chem. Rev.* **1998**, *98*, 2549.

(13) Anschutz, A. J.; Lee Penn, R. *Geochem. Trans.* **2005**, *6*, 60.

(14) Madden, A. S.; Hochella, J., M. F. *Geochim. Cosmochim. Acta* **2005**, *69*, 389.

(15) Stern, A. C.; Boubel, R. W.; Turner, D. B.; Fox, D. L. *Fundamentals of Air Pollution*, 2nd ed.; Academic Press: Orlando, FL, 1984.

(16) Al-Abadleh, H. A.; Grassian, V. H. *Surf. Sci. Rep.* **2003**, *52*, 63.

(17) Matsumoto, A.; Kaneko, K. *Colloids Surf.* **1989**, *37*, 81.

(18) Kaneko, K.; Matsumoto, A. *J. Phys. Chem.* **1989**, *93*, 8090.

particle size. For  $\text{SO}_2(\text{g})$  adsorption on  $\alpha\text{-FeOOH}$  nanoparticles in the range of 6–11 nm, only  $\text{SO}_3^{2-}$  was detected.<sup>18</sup>

The present study examines the interaction of  $\text{SO}_2(\text{g})$  with nanoferrhydrite. Unlike other iron hydroxides that have been studied, the exact structure and chemical composition of ferrhydrite is still a matter of debate.<sup>12</sup> The conventional classification of ferrhydrite is based on the number of X-ray diffraction (XRD) peaks. Normally a distinction is drawn between two types of ferrhydrite, referred to as 2-line and 6-line. In a typical XRD pattern of these materials, the 2-line form displays two broad peaks at 0.15 and 0.25 nm, while the more crystalline 6-line form displays six peaks at 0.15 (a doublet), 0.17, 0.20, 0.22, and 0.25 nm.<sup>12</sup> It has been proposed that the bulk structural unit for ferrhydrite is an  $\text{Fe}(\text{O},\text{OH})_6$  octahedron, while the surface structure is a mixture of octahedrally and tetrahedrally coordinated Fe.<sup>12,19</sup> The degree of crystallinity is determined by lengthening and polymerization of the dioctahedral chains to form a more coherent cross-linked structure.<sup>19,20</sup> In addition, 6-line ferrhydrite may be composed of small amounts of 2-line ferrhydrite.<sup>21</sup> The phase variations of ferrhydrite and the states of hydration and/or hydroxylation contribute to variable stoichiometries. For example, bulk compositions of the 2-line form are reported either as  $\text{Fe}_4(\text{O},\text{OH},\text{H}_2\text{O})_{12}$  or as  $\text{Fe}_6(\text{O},\text{OH},\text{H}_2\text{O})_{12}$ , with an Fe:O ratio ranging from 0.33 to 0.50.<sup>12</sup> Recent research from our laboratory using a pair distribution function (PDF) analysis of the total X-ray scattering from 2-line and 6-line ferrhydrite suggested that the coherent scattering domains share a common structure, albeit the average crystallite size and water content were different.<sup>22</sup>

In this investigation, nanoferrhydrite particles were synthesized with a narrow size distribution. Specifically, a biomimetic process was utilized to form well-dispersed supported monolayers of ferrhydrite.<sup>23–25</sup> Prior research has shown that ferritin (an iron storage protein), which is roughly a hollow sphere, can be used to assemble well-defined ferrhydrite nanoparticles within its interior.<sup>26</sup> In this contribution, mineralized ferritin was assembled on a support and the protein coat around the inorganic core was removed by exposing the system to reactive ozone, which oxidized the protein. This technique produced ferrhydrite particles with nominal sizes of 3 and 6 nm, which were characterized with transmission electron microscopy (TEM), atomic force microscopy (AFM), and scanning tunneling spectroscopy (STS). Nanoferrhydrite synthesized by traditional aqueous-based techniques (i.e., abiotic) was also investigated for comparative purposes. The surface chemistry and reactivity [ $\text{SO}_2(\text{g})$  sorption] was studied with attenuated total reflection Fourier transform infrared (ATR-FTIR) spectroscopy in combination with molecular orbital/density functional theory (MO/DFT) frequency calculations. Results showed that  $\text{SO}_2(\text{g})$  sorption may be a sensitive function of the structural properties and size of the nanoparticles.

## 2. Materials and Methods

**2.1. Synthesis and Sample Preparation.** Horse spleen ferritin (HSF) was obtained from Sigma–Aldrich (85 mg/mL, 0.15 M NaCl background electrolyte). HSF was demineralized to form apoferritin

as described elsewhere.<sup>23–25</sup> Individual apoferritin fractions were remineralized with loadings of 500 and 2000 Fe atoms/protein. Briefly, 500-Fe loaded ferritin was prepared by addition of 0.2 mL of deoxygenated ferrous ammonium sulfate solution [ $(\text{NH}_4)_2\text{Fe}(\text{SO}_4)\cdot 6\text{H}_2\text{O}$ , Sigma–Aldrich] (10 mg/mL) to 5 mg of apoferritin ( $2.5 \times 10^{-6}$  M, Sigma–Aldrich) in 20 mL of MES (0.1 M) at pH 6.5, followed by air oxidation. For the 2000-Fe loaded ferritin, four 0.2 mL aliquots of ferrous ammonium sulfate were added to apoferritin with intervals of 1 h between each addition. Remineralized ferritin was dialyzed in 0.1 M Tris buffer at pH 8.5. Apoferritin was mixed with the 500- and 2000-Fe loaded ferritin solutions at a 4:1 ratio and the mixtures were subsequently dialyzed in deionized water. Dilution of ferritin with apoferritin proved useful as a spacer to minimize aggregation of ferritin and ultimately the supported ferrhydrite particles.

For AFM and STM experiments, a single crystal of Au(111) (thickness 0.5 cm, diameter 1.0 cm, Monocrystal) was used as a substrate for the deposited ferritin. Atomically flat Au is a suitable substrate on which adsorbates can be deposited and characterized by STM and AFM.<sup>27</sup> Prior to each use, the Au crystal was sequentially cleaned with acetone and ethanol and with nitric acid, thoroughly rinsed with deionized water, and dried in an  $\text{N}_2(\text{g})$  jet. Immediately following cleaning, the Au crystal was annealed in a hydrogen flame. Both STM and AFM images showed an atomically smooth Au surface with terrace widths of 100–200 nm (obtained routinely). AFM and STM samples were prepared by spreading 30  $\mu\text{L}$  of a 0.1 mg/mL mixture of apoferritin/remineralized ferritin on the Au substrate. Excess solution on the Au(111) surface was removed by absorption with filter paper. Various concentrations of apoferritin/remineralized ferritin mixtures ranging from 0.01 to 1 mg/mL were tested, and 0.1 mg/mL was optimal for AFM and STM measurements.

TEM samples were prepared by spreading a drop of apoferritin/remineralized ferritin solution (0.1 mg/mL) onto an amorphous carbon film supported by a standard TEM grid. Excess solution was removed with filter paper and the grid was dried in an  $\text{N}_2(\text{g})$  jet at room temperature. ATR-FTIR samples were prepared by spreading 100  $\mu\text{L}$  of 0.2 mg/mL apoferritin/remineralized ferritin onto a ZnSe ATR crystal, with subsequent drying in a  $\text{N}_2(\text{g})$  jet. Finally, all the supported remineralized ferritin samples were exposed to a UV–ozone (Novascan) cleaner for 60 min at 373 K, a temperature well below the phase transition of ferrhydrite to hematite.<sup>12</sup> This led to removal of the ferritin protein shell and left isolated nanoparticles on each surface.<sup>25,28</sup> Apoferritin that was used as a spacer (to separate mineralized ferritin on each support) was removed during this cleaning step.

To compare ferrhydrite nanoparticles assembled in ferritin with traditionally synthesized ferrhydrite nanoparticles, 2-line ferrhydrite was synthesized by a nonbiological route detailed elsewhere.<sup>12</sup> Briefly, 2-line ferrhydrite nanoparticles were synthesized by adding 1 M solution of reagent-grade potassium hydroxide (Sigma–Aldrich) to a 0.2 M solution of reagent-grade ferric nitrate (Sigma–Aldrich) with constant stirring until the pH reached 7.5. The precipitate was repeatedly washed with deionized water and centrifuged to remove electrolytes.

**2.2. Characterization.** Tapping-mode AFM (TM-AFM) measurements were performed under ambient conditions on a PicoSPM II (Molecular Imaging). The probes used in all measurements were NSC15 ( $\mu\text{Masch}$ ) with a nominal spring constant of 40 N/m and a resonant frequency of 325 kHz.

STM measurements were also performed on a PicoSPM II (Molecular Imaging) under constant current mode in an environmental chamber filled with dry  $\text{N}_2(\text{g})$ . Probes were mechanically cut from 80% Pt/20% Ir wires. The current–voltage ( $I$ – $V$ ) curves of individual and isolated particles were obtained by positioning the STM tip over a selected particle while the feedback loop of the microscope was turned off. Typically, recorded spectra were the sum of 80 individual curves.

(19) Gloter, A.; Zbinden, M.; Guyot, F.; Gaill, F.; Colliex, C. *Earth Planet. Sci. Lett.* **2004**, *222*, 947.

(20) Waychunas, G. A.; Fuller, C.; Rea, B. A.; Davis, J. A. *Geochim. Cosmochim. Acta* **1996**, *60*, 1765.

(21) Janney, D. E.; Cowley, J. M.; Buseck, P. R. *Am. Mineral.* **2001**, *86*, 327.

(22) Michel, M. F.; Antao, S. M.; Celestian, A. J.; Ehm, L.; Schoonen, M. A. A.; Parise, J. B.; Liu, G.; Strongin, D. R.; Kim, J.; Grey, C. P.; Han, W.; Gillow, J.; Chupas, P. J.; Lee, P. L. *Chem. Mater.* **2006** (submitted for publication).

(23) Wong, K. K. W.; Douglas, T.; Gider, S.; Awschalom, D. D.; Mann, S. *Chem. Mater.* **1998**, *10*, 279.

(24) Allen, M.; Willits, D.; Young, M.; Douglas, T. *Inorg. Chem.* **2003**, *42*, 6300.

(25) Hosein, H.-A.; Strongin, D. R.; Allen, M.; Douglas, T. *Langmuir* **2004**, *20*, 10283.

(26) Douglas, T. *Biomimetic Mater. Chem.* **1996**, 91.

(27) Poirier, G. E. *Langmuir* **1999**, *15*, 1167.

(28) Hikono, T.; Uraoka, Y.; Fuyuki, T.; Yamashita, I. *Jpn. J. Appl. Phys.* **2003**, *42*, L398.

Powder XRD data were collected at beamline 11-IDB (90 keV,  $\lambda = 0.1349(2) \text{ \AA}$ )<sup>29</sup> of the Advanced Photon Source, Argonne National Laboratory. Two-line ferrihydrite nanoparticles (nonbiological synthetic route) were loaded as semidry powders into 1 mm (o.d.) polyimide (Kapton) capillaries. Radiation scattered by the samples was collected with a MAR-345 image plate detector system and processed with Fit-2D.<sup>30,31</sup> A polarization correction was applied during integration of the data. Data were also collected on a blank polyimide capillary (i.e., control) for background correction. The sample capillary was rotated during data collection.

TEM images and selected area electron diffraction (SAED) patterns were obtained on a JEOL-3000 F with the electron source operating at 300 keV. An energy-dispersive X-ray spectrometer (EDS) was attached to the TEM. Chemical composition of the nanoparticles was O and Fe, as confirmed by both EDS and X-ray spectroscopy (XPS).<sup>25</sup>

**2.3. SO<sub>2</sub> Sorption.** Infrared spectra were recorded on a Nicolet Magna 560 IR spectrometer, equipped with a N<sub>2</sub>(l)-cooled narrow bandwidth mercury–cadmium–telluride (MCT-A) detector. Single-beam spectra were recorded by averaging 1500 scans at 4 cm<sup>-1</sup> resolution in the spectral range 650–4000 cm<sup>-1</sup>. A 45° horizontal ZnSe ATR crystal (thickness 6 mm; dimension of the larger upper face 10 × 70 mm; five internal reflections) was used. All reported ATR-FTIR spectra were referenced to the ZnSe crystal coated with ferrihydrite nanoparticles. A commercial N<sub>2</sub>(g) dryer was used to purge the FTIR spectrometer optics and internal compartment. Prior to the infrared measurements, the samples were further dried by exposure to dry N<sub>2</sub>(g) for approximately 10 min. The dosing of high-purity sulfur dioxide (Matheson, 99.98 wt % purity) was performed in a flow system at room temperature. Samples were exposed to SO<sub>2</sub>(g) (~760 Torr) for 15 min. After 15 min of exposure, the IR cell was sealed with SO<sub>2</sub>(g) inside. SO<sub>2</sub>(g) was used as received from the manufacturer, without further purification.

Frequency calculations were performed with the electronic structure program Gaussian 03.<sup>32</sup> The unrestricted, hybrid density functional method was employed by use of Becke's three-parameter nonlocal-exchange functional<sup>33,34</sup> with the gradient-corrected correlation functional of Lee, Yang, and Parr<sup>35</sup> (UB3LYP). The standard 6-31+G(d) all-electron basis set was used. Minima on the potential energy surfaces were located from a geometry optimization on the entire system with no symmetry or geometrical constraints being allowed. Frequency calculations were subsequently performed on the geometry-optimized structures to verify that a minimum was successfully located (i.e., no imaginary frequencies) and to obtain predicted IR frequencies comparable to experimental ATR-FTIR spectra. For each calculation, the high-spin state of Fe(III) ( $s = 5/2$ ) was specified.

(29) Rutt, U.; Beno, M. A.; Stempfer, J.; Jennings, G.; Kurtz, C.; Montano, P. A. *Nucl. Instr. Methods A* **2001**, *467*, 1026.

(30) Hammersley, A. P. ESRF Internal Report ESRF98HA01T, 1998.

(31) Hammersley, A. P.; Svensson, S. O.; Hanfland, M.; Fitch, A. N.; Hausermann, D. *High Pressure Res.* **1996**, *14*, 235.

(32) Frisch, M. J.; Trucks, G. W.; Schlegel, H. B.; Scuseria, G. E.; Robb, M. A.; Cheeseman, J. R.; Montgomery, J. A., Jr.; Vreven, T.; Kudin, K. N.; Burant, J. C.; Millam, J. M.; Iyengar, S. S.; Tomasi, J.; Barone, V.; Mennucci, B.; Cossi, M.; Scalmani, G.; Rega, N.; Petersson, G. A.; Nakatsuji, H.; Hada, M.; Ehara, M.; Toyota, K.; Fukuda, R.; Hasegawa, J.; Ishida, M.; Nakajima, T.; Honda, Y.; Kitao, O.; Nakai, H.; Klene, M.; Li, X.; Knox, J. E.; Hratchian, H. P.; Cross, J. B.; Bakken, V.; Adamo, C.; Jaramillo, J.; Gomperts, R.; Stratmann, R. E.; Yazyev, O.; Austin, A. J.; Cammi, R.; Pomelli, C.; Ochterski, J. W.; Ayala, P. Y.; Morokuma, K.; Voth, G. A.; Salvador, P.; Dannenberg, J. J.; Zakrzewski, V. G.; Dapprich, S.; Daniels, A. D.; Strain, M. C.; Farkas, O.; Malick, D. K.; Rabuck, A. D.; Raghavachari, K.; Foresman, J. B.; Ortiz, J. V.; Cui, Q.; Baboul, A. G.; Clifford, S.; Cioslowski, J.; Stefanov, B. B.; Liu, G.; Liashenko, A.; Piskorz, P.; Komaromi, I.; Martin, R. L.; Fox, D. J.; Keith, T.; Al-Laham, M. A.; Peng, C. Y.; Nanayakkara, A.; Challacombe, M.; Gill, P. M. W.; Johnson, B.; Chen, W.; Wong, M. W.; Gonzalez, C.; Pople, J. A. *Gaussian 03*, revisions B.02 and C.01; Gaussian, Inc.: Wallingford, CT, 2004.

(33) Stephens, P. J.; Devlin, F. J.; Chabalowski, C. F.; Frisch, M. J. *J. Phys. Chem.* **1994**, *98*, 11623.

(34) Becke, A. D. *J. Chem. Phys.* **1993**, *98*, 5648.

(35) Lee, C. T.; Yang, W. T.; Parr, R. G. *Phys. Rev. B* **1988**, *37*, 785.

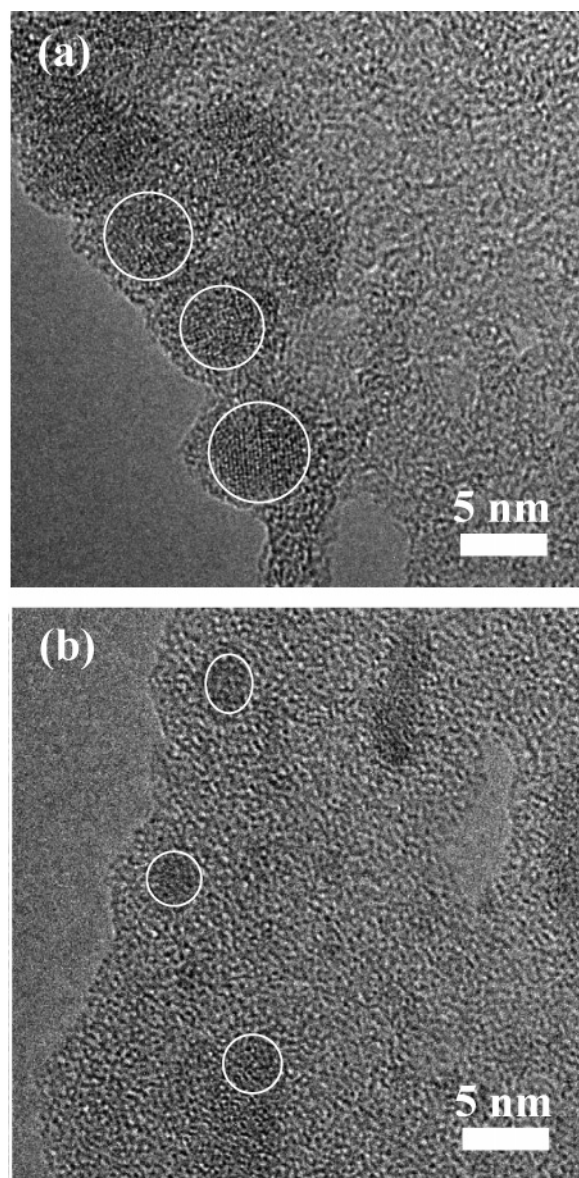


**Figure 1.** TEM images of ferrihydrite nanoparticles with (a) 2000 and (b) 500 Fe atoms/particle. White circles highlight the nanoparticles.

### 3. Results

**3.1. TEM.** A representative TEM image of the nanoparticles containing 2000 Fe atoms is displayed in Figure 1. The nanoparticles were relatively uniform with regard to size and shape. The lattice spacing was measured at 0.255 nm, in agreement with the lattice spacing of ferrihydrite measured by XRD and previous TEM results.<sup>36</sup> All nanoparticles examined with resolvable lattice fringes exhibited a single domain structure. TEM images showed that most particles were lattice-resolvable, indicating that the particles with 2000 Fe atoms had well-defined crystallinity. The average diameter of the nanoparticles was  $6.5 \pm 0.9$  nm, based on an analysis of 100 individual particles. When inorganic and mineral materials are imaged by high-resolution electron microscopy, it should be noted that structural transitions induced by electron irradiation could occur under certain circumstances.<sup>37</sup> In the present work, an area was examined and

(36) Quintana, C.; Cowley, J. M.; Marhic, C. *J. Struct. Biol.* **2004**, *147*, 166.

(37) Hobbs, L. W. Radiation effects in analysis of inorganic specimens by TEM. In *Introduction to Analytical Electron Microscopy*, Hren, J. J., Goldstein, J. L., Joy, D. C., Eds.; Plenum: New York, 1979; pp 437–480.

TEM images were collected within a few minutes. No evidence of structural transformations, such as a crystalline to amorphous phase transition, was observed.

Figure 1 also displays a representative TEM image of the nanoparticles containing 500 Fe atoms. The image shows that most of the particles exhibited irregular shapes and were relatively amorphous (lacking lattice structure), suggesting an early stage of particle growth. This observation was in contrast to the nanoparticles consisting of approximately 2000 Fe atoms, which were more crystalline. Analysis of the TEM micrographs indicated that most nanoparticles were amorphous, and the lack of diffraction spots in SAED patterns (not shown here) was consistent with the majority of the particles being highly disordered. The particles did, however, have a narrow size distribution with an average diameter of  $2.6 \pm 0.8$  nm, as evidenced by TEM analysis of 100 particles.

**3.2. Scanning Probe Microscopy.** **3.2.1. AFM.** Figure 2 displays AFM topographical and phase images of ferrihydrite nanoparticles composed of 500 Fe atoms/particle deposited on Au(111). After drop casting followed by UV–ozone treatment, a high density of roughly spherical ferrihydrite nanoparticles was observed on the surface. Close inspection of the 500-Fe atom/particle images, collected from different parts of the sample surface, showed an average particle diameter of  $3 \pm 0.5$  nm (more than 100 particles), consistent with the TEM measurements. AFM analysis was based on the  $z$ -dimension (or height) of an individual particle, since the lateral resolution of the particle determined by the radius of curvature and sidewall angles of the AFM tip, exaggerates the true particle size.<sup>38</sup>

**3.2.2. STM.** Figure 3 shows a high-resolution STM image of individual particles containing a mixture of 500 and 2000 Fe atoms deposited on Au(111). In contrast to the lower lateral resolution images obtained by AFM, STM images showed that the particle morphology was quite rough on the atomic scale. STM images suggested that the particle surfaces were heterogeneous and may exhibit a high density of low-coordinated sites, such as edges and kinks.

To probe the electronic structure of individual particles, STS measurements were performed. STS provides a spectroscopic tool for investigation of surface electronic structure, such as local density of states and band gaps of semiconductor materials.<sup>39</sup> Figure 3 shows STS data corresponding to an individual particle containing either 500 or 2000 Fe atoms. A linear (ohmic)  $I$ – $V$  curve was always measured between the metallic STM tip and bare Au(111) substrate (data not shown). In contrast, particle A (2000 Fe atoms) with a height of 6 nm exhibited a band gap of  $\sim 2.7$  eV, while particle B (500 Fe atoms) with a height of 3 nm exhibited a band gap of  $\sim 1.5$  eV. These values were obtained from the voltage range in which there was zero tunneling current. Similar results were reproduced on 50 individual particles, and the different band gaps are proposed to be associated with structural differences (perhaps at the surface, where STM is probing) between the 500 and 2000 Fe atom particles. These differences are not totally unexpected, considering that TEM results indicated the two different particle sizes had significantly different crystallinity. Furthermore, differences in the concentration of structural or surface water of the ferrihydrite nanoparticles could influence the STS results.<sup>40</sup>

**3.3. XRD and TEM of 2-Line Ferrihydrite.** A limited amount of characterization was carried out on ferrihydrite nanoparticles

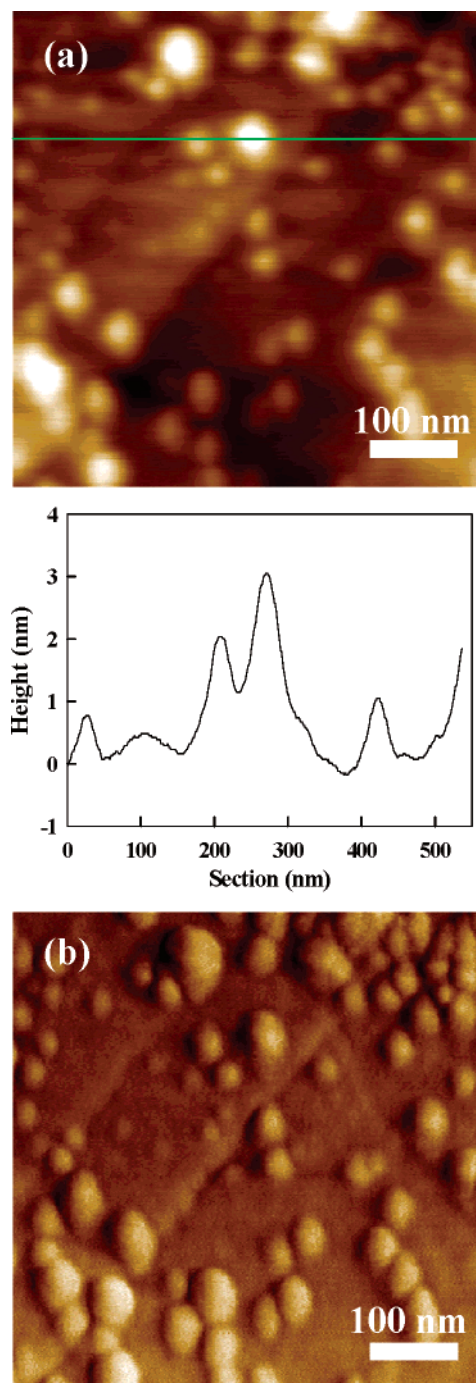


**Figure 2.** TM-AFM topographical (a) and phase (b) images ( $550 \times 550$  nm) of ferrihydrite nanoparticles (500 Fe atoms/particle) deposited on Au(111). The cross-sectional view corresponds to the line drawn in the image.

synthesized by precipitation from solution without the aid of ferritin. Figure 4 exhibits an XRD pattern for this material consistent with 2-line ferrihydrite, where the diffraction pattern was characterized by two dominant peaks.<sup>41</sup> The corresponding TEM image in Figure 4 shows that the particle diameter for this material ranged from 2 to 4 nm. The inset SAED pattern in the figure displays two broad rings at 0.148 and 0.253 nm, consistent with 2-line ferrihydrite.<sup>42</sup> In terms of morphology and size, synthetic 2-line ferrihydrite nanoparticles were more similar to ferrihydrite nanoparticles containing 500 Fe atoms.

(38) García, R.; Pérez, R. *Surf. Sci. Rep.* **2002**, *47*, 197.

(39) Wiesendanger, R., *Scanning Tunneling Microscopy—Analytical Methods (NanoScience and Technology)*; Springer: Berlin, 1998.

(40) Maurice, V.; Fremy, N.; Marcus, P. *Surf. Sci.* **2005**, *581*, 88.

(41) Pannalal, S. J.; Crowe, S. A.; Cioppa, M. T.; Symons, D. T. A.; Sturm, A.; Fowle, D. A. *Earth Planet. Sci. Lett.* **2005**, *236*, 856.

(42) Greffié, C.; Amouric, M.; Parron, C. *Clay Miner.* **2001**, *36*, 381.

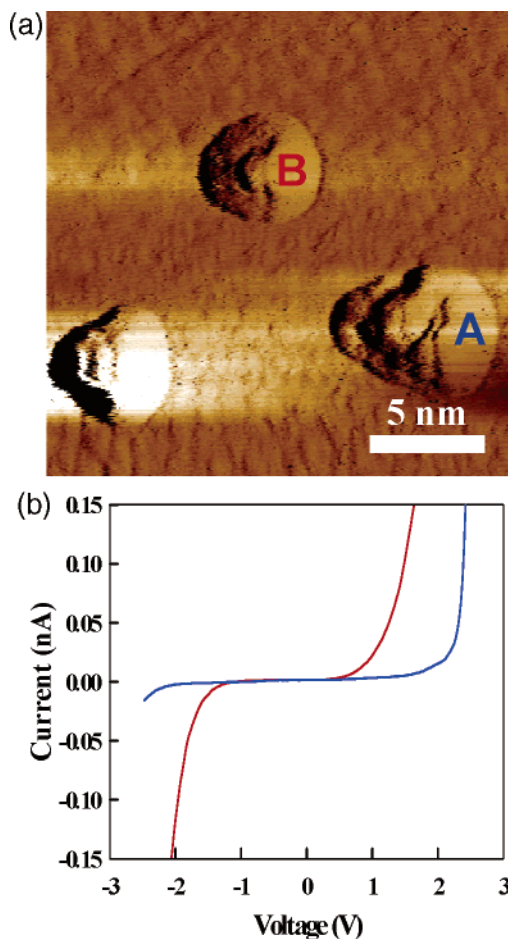


**Figure 3.** Representative STM image ( $20 \times 20$  nm) (a) and STS spectra (b) of nanoparticles containing 2000 (blue line, A) and 500 (red line, B) Fe atoms per particle.

**3.4. ATR-FTIR of  $\text{SO}_2(\text{g})$  Sorption.** Reaction of  $\text{SO}_2(\text{g})$  with ferritin-assembled and reference ferrihydrite nanoparticles was investigated by ATR-FTIR spectroscopy. Interpretation of the IR spectra was facilitated with MO/DFT frequency calculations. Calculated frequencies for a variety of sulfur oxyanion species [(bi)sulfate<sup>43</sup> and (bi)sulfite] coordinated to a model Fe–(hydr)-oxide cluster are listed in Table 1, and a selected group of corresponding geometry-optimized structures are shown in Figure 5. Note that not every conceivable adsorption complex was modeled, but IR frequencies were calculated for commonly observed coordination geometries of sulfur oxyanion species found in similar systems.<sup>17,18,44,45</sup> Figure 6 shows IR spectra corresponding to  $\text{SO}_2(\text{g})$  exposure for 1 h. IR spectra collected as a function of  $\text{SO}_2(\text{g})$  exposure time are shown in Figure 7. Spectra were collected until no further changes in the intensity or position of the vibrational modes were experimentally observed (60 h maximum). Possible assignments for the experimentally observed frequencies, based upon calculated frequencies, are given in Table 2. Consistent with prior experimental observations,<sup>45,46</sup> the calculations show in general that sulfite contributes mode intensity below  $1100 \text{ cm}^{-1}$  and sulfate exhibits modes above this energy.

IR spectra shown in Figure 7 illustrate the degree of complexity associated with the reaction of  $\text{SO}_2(\text{g})$  and ferrihydrite nano-

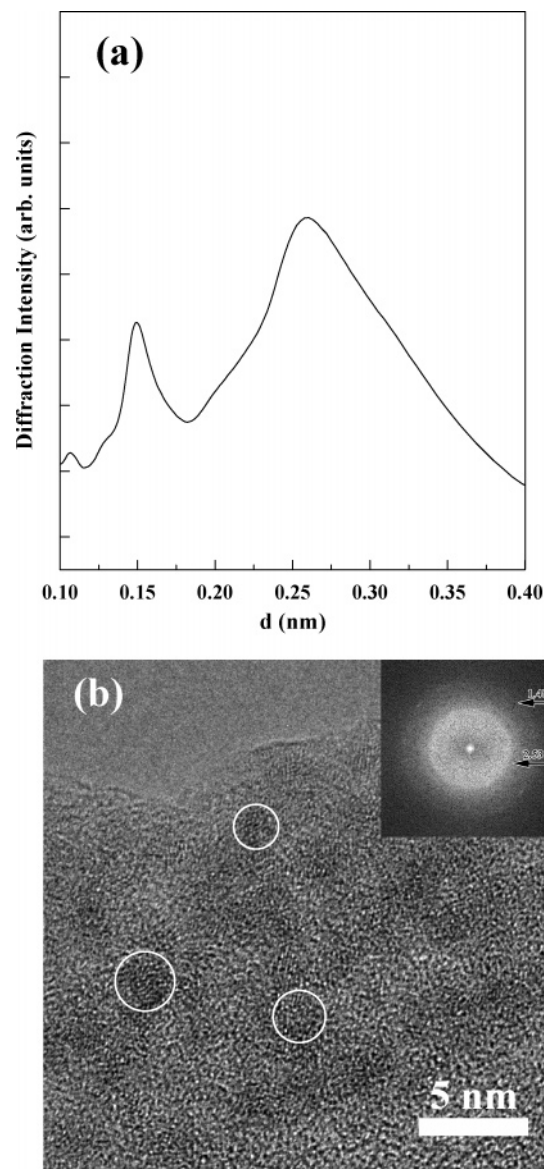


**Figure 4.** (a) Powder XRD pattern of synthetic 2-line ferrihydrite nanoparticles. (b) TEM image and SAED pattern of synthetic 2-line ferrihydrite nanoparticles. White circles indicate the ferrihydrite nanoparticles. (Inset) Electron diffraction pattern.

particles. The type of surface species observed on the nanoparticles was a function of  $\text{SO}_2(\text{g})$  exposure time.  $\text{SO}_2(\text{g})$  was converted to  $\text{SO}_3^{2-}$  surface complexes, a fraction of which may have subsequently oxidized to  $\text{SO}_4^{2-}$  (minor surface complex). After 60 h, all three species were experimentally observed, although their respective surface concentrations varied on different ferrihydrite nanoparticles. Due to the complexity arising from a mixture of adsorbed complexes, tentative assignments of the major vibrational frequencies (high intensity) in the IR spectra were made with the aid of MO/DFT calculated frequencies (minor, low-intensity frequencies possibly associated with  $\text{SO}_3^{2-}$  oxidation to  $\text{SO}_4^{2-}$  were also tentatively assigned). Assignments listed in Table 2 suggest that observed sulfur oxyanion complexes were similar on the different nanoparticle surfaces, though their relative concentration varied. The vibrational frequencies associated with a particular species on the ferrihydrite nanoparticles differed by less than  $10 \text{ cm}^{-1}$  (Table 2). However, the relative intensities of the vibrational frequencies were different, implying that the distribution of sulfur oxyanion species was sensitive to the surface structure and/or hydration state of the nanoparticle.

(43) Paul, K. W.; Borda, M. J.; Kubicki, J. D.; Sparks, D. L. *Langmuir* **2005**, *21*, 11071.

(44) Hug, S. J. *J. Colloid Interface Sci.* **1997**, *188*, 415.

(45) Goodman, A. L.; Li, P.; Usher, C. R.; Grassian, V. H. *J. Phys. Chem. A* **2001**, *105*, 6109.

(46) Ziolek, M.; Kujawa, J.; Saur, O.; Aboulayt, A.; Lavalley, J. C. *J. Mol. Catal. A* **1996**, *112*, 125.

**Table 1.** Calculated Vibrational Frequencies of Potential Energy-Minimized (bi)Sulfate and (bi)Sulfite Surface Complexes on Fe-(hydr)Oxide Clusters<sup>a</sup>

sulfate		sulfite		
monodentate	bidentate	monodentate <sup>b</sup>	monodentate <sup>c</sup>	bidentate
1139 (338)	1143 (468)			
	1070 (423)	1072 (176)	1076 (131)	
1029 <sup>d</sup>	1003 <sup>d</sup>	1036 (176)	1030 (290)	1010 (333)
		972 (133)		
942 (171)	937 (45)		917 (237)	
				869 (467)
				818 (334)
bisulfate		bisulfite		
monodentate	bidentate	bidentate		
1222 (307)	1236 (347)			
1174 (282)	1152 (317)			
1105 (238)	1119 (243)	1119 (131)		
		1058 (392)		
1011 (294)	1012 (266)	1012 (185)		

<sup>a</sup> Frequencies are given as wavenumbers ( $\text{cm}^{-1}$ ), and intensities are listed in parentheses. Values are reported for normal modes between 800 and  $1300\text{ cm}^{-1}$ . UB3LYP/6-31G+(d) was used for calculations.

<sup>b</sup> Monodentate sulfite H-bonded to next-nearest-neighbor OH functional group. <sup>c</sup> Monodentate sulfite H-bonded to next-nearest-neighbor OH functional group and bridging OH between Fe atoms. <sup>d</sup> Intensity-weighted average of two identical normal modes.

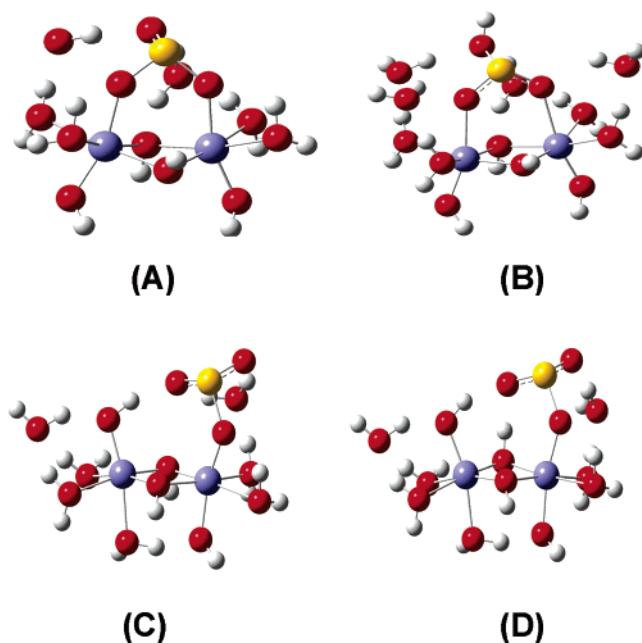


**Figure 5.** Potential energy-minimized (bi)sulfite adsorption complexes on Fe(III)-(hydr)oxide clusters: (A) sulfite bidentate; (B) bisulfate bidentate; (C) sulfite monodentate H-bonded to next-nearest-neighbor OH functional group; (D) sulfite monodentate H-bonded to next-nearest-neighbor OH functional group and bridging OH between Fe atoms. Red, oxygen; white, hydrogen; yellow, sulfur; blue, iron.

The most intense bands at  $1144$  and  $1330\text{ cm}^{-1}$  (Figure 6) were assigned to the symmetric ( $\nu_1$ ) and asymmetric ( $\nu_3$ ) stretching modes of adsorbed  $\text{SO}_2(\text{g})$ , respectively. These particular bands were shifted from their corresponding gas-phase values of  $1154$  and  $1360\text{ cm}^{-1}$ .<sup>47</sup> Additional experiments showed that upon evacuation of  $\text{SO}_2(\text{g})$  from the reaction cell these two bands remained, suggesting that they corresponded to a strongly

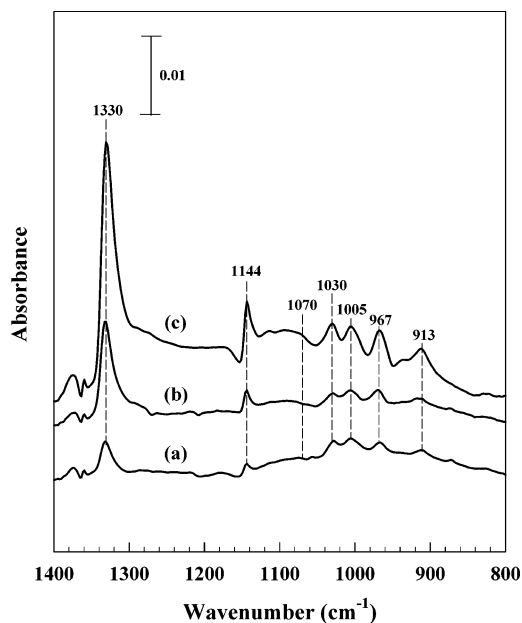


**Figure 6.** Comparison of ATR-FTIR spectra ( $1400\text{--}800\text{ cm}^{-1}$ ) of nanoparticles: (a) 2000 Fe atoms/particle; (b) 500 Fe atoms/particle assembled in ferritin, and (c) synthetic 2-line ferrihydrite nanoparticles, following exposure to gas-phase  $\text{SO}_2$  for 1 h.

chemisorbed species.<sup>45</sup> Except for  $\text{SO}_2$ , measured bands corresponding to sulfur oxyanion products grew with  $\text{SO}_2(\text{g})$  exposure time (Figure 7). IR spectra (Figures 6 and 7) show several intense vibrational frequencies ( $1070$ ,  $1030$ ,  $1005$ ,  $968$ , and  $910\text{ cm}^{-1}$ ), which on the basis of our calculations (Table 1) were assigned to monodentate and bidentate bridging  $\text{SO}_3^{2-}$ .

The bidentate bridging  $\text{SO}_3^{2-}$  calculated vibrational mode at  $1010\text{ cm}^{-1}$  closely approximated the intense experimental band at  $1005\text{ cm}^{-1}$  (Tables 1 and 2, Figure 7). The bidentate bridging  $\text{SO}_3^{2-}$  frequency calculation also predicted two vibrational modes between  $800$  and  $900\text{ cm}^{-1}$  (Table 1). Two relatively weak experimental frequencies at approximately  $820$  and  $875\text{ cm}^{-1}$  agreed well with the calculated frequencies at  $818$  and  $869\text{ cm}^{-1}$ , respectively (Tables 1 and 2, Figure 7). Monodentate  $\text{SO}_3^{2-}$  appeared to be the dominant surface species present in each of the three systems investigated. Calculated monodentate  $\text{SO}_3^{2-}$  asymmetric stretching modes at approximately  $1070$  and  $1030\text{ cm}^{-1}$  agreed well with measured bands at approximately  $1075$  and  $1030\text{ cm}^{-1}$ , respectively (Tables 1 and 2). Interestingly, it was determined that the symmetric stretching mode of monodentate  $\text{SO}_3^{2-}$  was quite sensitive to the local H-bonding environment, though the two asymmetric stretching modes were not (Table 1). When monodentate  $\text{SO}_3^{2-}$  H-bonded with a next-nearest-neighbor surface OH functional group, the calculated symmetric stretching mode was equal to  $972\text{ cm}^{-1}$  (Table 1, Figure 5C). However, when monodentate  $\text{SO}_3^{2-}$  H-bonded with the next-nearest-neighbor surface OH functional group and the bridging OH between the two Fe atoms, the symmetric stretching mode was significantly red-shifted to  $917\text{ cm}^{-1}$  (Table 1, Figure 5D). Frequency calculations involving either two or four H-bonding interactions with bidentate bridging  $\text{SO}_3^{2-}$  revealed insignificant changes (data not shown), suggesting that this coordination complex was less sensitive to the local H-bonding environment (Figure 5A, H-bonding with two waters).

It is plausible that the heterogeneous surfaces of the ferrihydrite nanoparticles allow for variability in surface complexation, particularly for monodentate  $\text{SO}_3^{2-}$  coordination. If this variability indeed exists, monodentate  $\text{SO}_3^{2-}$  complexes may be able to adopt slightly different geometries on a single nanoparticle

(47) Herzberg, G. *Molecular Spectra and Molecular Structure*; Van Nostrand: Princeton, NJ, 1950; Vol. 1.

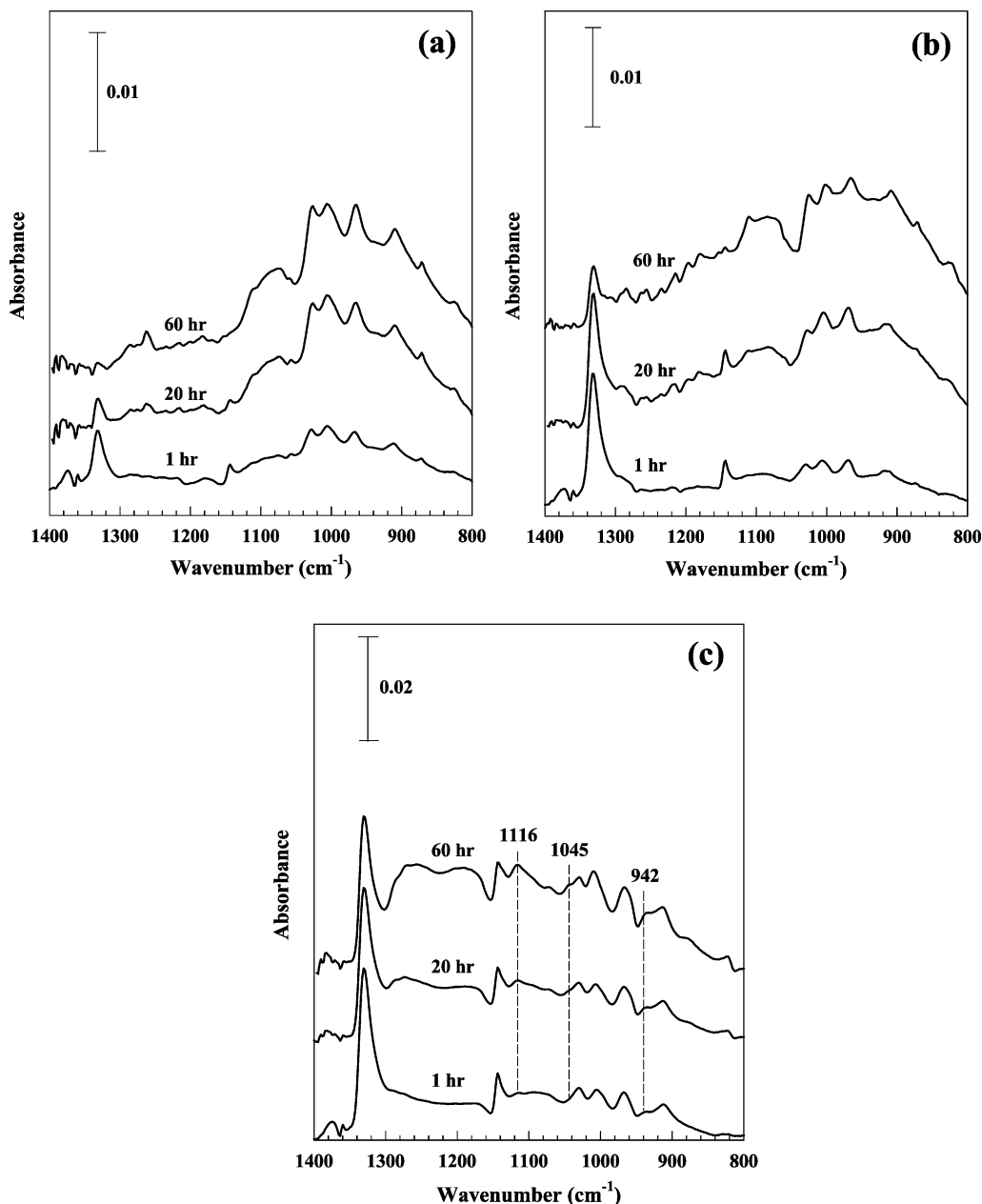


**Figure 7.** ATR-FTIR spectra ( $1400\text{--}800\text{ cm}^{-1}$ ) of nanoparticles assembled in ferritin: (a) 2000 Fe atoms/particle; (b) 500 Fe atoms/particle; and (c) synthetic 2-line ferrihydrite nanoparticles, following exposure to gas-phase  $\text{SO}_2$ .

**Table 2. Potential Assignment of Experimental IR Frequencies Corresponding to  $\text{SO}_2$  Sorption Products<sup>a</sup>**

2000 Fe atoms/particle	500 Fe atoms/particle	synthetic 2-line ferrihydrite
1332 ( $\text{SO}_2$ )	1332 ( $\text{SO}_2$ )	1330 ( $\text{SO}_2$ )
1144 ( $\text{SO}_2$ )	1144 ( $\text{SO}_2$ )	1144 ( $\text{SO}_2$ )
1113 ( $\text{SO}_4^{2-}$ , m)	1112 ( $\text{SO}_4^{2-}$ , m)	1116 ( $\text{SO}_4^{2-}$ , m)
1074 ( $\text{SO}_3^{2-}$ , m)	1082 ( $\text{SO}_3^{2-}$ , m)	1072 ( $\text{SO}_3^{2-}$ , m)
1045 ( $\text{SO}_4^{2-}$ , m)	1045 ( $\text{SO}_4^{2-}$ , m)	1045 ( $\text{SO}_4^{2-}$ , m)
1028 ( $\text{SO}_3^{2-}$ , m)	1028 ( $\text{SO}_3^{2-}$ , m)	1030 ( $\text{SO}_3^{2-}$ , m)
1005 ( $\text{SO}_3^{2-}$ , bb)	1005 ( $\text{SO}_3^{2-}$ , bb)	1005 ( $\text{SO}_3^{2-}$ , bb)
966 ( $\text{SO}_3^{2-}$ , m)	969 ( $\text{SO}_3^{2-}$ , m)	967 ( $\text{SO}_3^{2-}$ , m)
942 ( $\text{SO}_4^{2-}$ , m)	942 ( $\text{SO}_4^{2-}$ , m)	942 ( $\text{SO}_4^{2-}$ , m)
910 ( $\text{SO}_3^{2-}$ , m)	910 ( $\text{SO}_3^{2-}$ , m)	913 ( $\text{SO}_3^{2-}$ , m)
875 ( $\text{SO}_3^{2-}$ , bb)	875 ( $\text{SO}_3^{2-}$ , bb)	875 ( $\text{SO}_3^{2-}$ , bb)
820 ( $\text{SO}_3^{2-}$ , bb)	820 ( $\text{SO}_3^{2-}$ , bb)	820 ( $\text{SO}_3^{2-}$ , bb)

<sup>a</sup> Frequencies are given as wavenumbers ( $\text{cm}^{-1}$ ). m and bb refer to monodentate and bidentate bridging, respectively.

(perhaps even on a single crystal face). For example, the experimental bands measured at approximately  $966$  and  $910\text{ cm}^{-1}$

could both be assigned as monodentate  $\text{SO}_3^{2-}$  symmetric stretching modes (Table 2), given the calculated range of this vibrational mode (Table 1). Alternatively, the bands measured at approximately  $966$  and  $910\text{ cm}^{-1}$  may belong to two different surface species. If this is the case, the exact nature of the unique surface complexes remains to be elucidated. Furthermore, to simplify data analysis, MO/DFT calculations were not performed for sulfite/sulfate adsorption complexes possibly occurring on tetrahedral Fe surface sites. Adsorption at these types of sites may be contributing to modes that cannot at this time be identified based upon frequency calculations (e.g. possibly one of the two bands at  $966$  or  $910\text{ cm}^{-1}$ ).

Several low-intensity bands were observed to grow as a function of  $\text{SO}_2(\text{g})$  exposure time. Figure 7 shows that the largest amount of  $\text{SO}_2(\text{g})$  sorption occurred for the synthetic 2-line ferrihydrite nanoparticles (see inset intensity scales in each figure). Three bands at approximately  $1113$ ,  $1045$ , and  $942\text{ cm}^{-1}$  grew in intensity as a function of  $\text{SO}_2(\text{g})$  exposure time and were

tentatively assigned to monodentate sulfate (Tables 1 and 2). It is possible that a small quantity of O<sub>2</sub>(g) impurity entered the reaction cell over time in these experiments and promoted SO<sub>3</sub><sup>2-</sup> oxidation to SO<sub>4</sub><sup>2-</sup> on the ferrihydrite nanoparticles. It is difficult to imagine that Fe(III) was reduced to Fe(II) by SO<sub>3</sub><sup>2-</sup>, though this could not be experimentally determined. Nevertheless, the concentration of SO<sub>4</sub><sup>2-</sup> surface complexes is quite low given its associated low-intensity vibrational frequencies. For all three types of nanoparticles, weak bands between 1150 and 1300 cm<sup>-1</sup> were observed but were not assigned, given the low signal-to-noise resolution in this region.

#### 4. Discussion

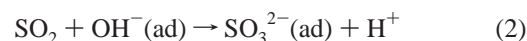
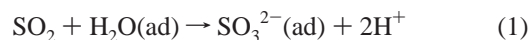
Using electron nanodiffraction, Cowley et al.<sup>48</sup> studied native ferritin cores with an average diameter of 8 nm. They reported that the majority of mineralized native ferritin displayed a crystalline structure similar to that of 6-line ferrihydrite, while a minor fraction exhibited a highly disordered structure. Our results for remineralized ferritin were in reasonable agreement with prior work, since TEM showed a crystalline particle in the case of the larger 2000-Fe atoms/particle derived from ferritin (protein-removed) that was analogous to 6-line ferrihydrite. In contrast, the smaller particle (500-Fe atoms/particle) showed a relatively amorphous structure that was more consistent with 2-line ferrihydrite. In contrast to prior investigations on ferritin, the present results were obtained for particles heated to 373 K in an oxidizing environment to remove the protein shell. The conversion of powder ferrihydrite (not in aqueous solution) to other iron oxide phases such as hematite, however, is expected to require temperatures near 473 K.<sup>49</sup> It is interesting that the crystallinity of 3 and 6 nm particles assembled in ferritin showed a marked difference. Prior research on the mineralization of ferrihydrite in ferritin suggested a stepwise growth mechanism: (1) initial growth of the seed particle controlled by interior catalytic sites of the protein and (2) subsequent growth of the particle on the seed particle not regulated by the protein structure.<sup>50,51</sup> The smaller amorphous particles may be more representative of the initial seeding process in ferritin, and the larger crystalline particles may result from the protein-independent mineralization process.

STM/STS results were consistent with TEM results regarding the two different particle sizes investigated. STS measurements showed that the band gap of the 3 nm particles was less than 2 eV, while the larger, more crystalline particles exhibited a band gap above 2.5 eV, similar to the optical band gap of bulk iron oxide phases.<sup>52</sup> Using STM/STS and XPS, Preisinger et al.<sup>53</sup> studied nanosized iron oxides derived from native ferritin. Several different phases of iron oxide nanoparticles, such as  $\gamma$ -Fe<sub>2</sub>O<sub>3</sub>,  $\alpha$ -Fe<sub>2</sub>O<sub>3</sub>, and mixed phases with  $\gamma$ -Fe<sub>2</sub>O<sub>3</sub> and  $\alpha$ -Fe<sub>2</sub>O<sub>3</sub>, were prepared by thermal treatment and subsequent oxidation and/or reduction. For 7–8 nm nanoparticles supported on graphite, STS measurements showed that the band gap could vary between 1.3 and 2 eV, from particle to particle or even between different tunneling locations on an individual particle. The lower band gap, compared with bulk phases, was ascribed to defects at the surface, and we likewise attribute the lower band gap of the relatively amorphous particles (500 Fe atoms/particle) to a high

population of defect sites. Indeed, the unusually high catalytic activity for low-temperature CO oxidation of supported Au nanoparticles is argued to be due to undercoordinated gold atoms in corner or edge sites.<sup>54,55</sup> Similar structural changes are expected for oxide particles in the nanoregime, although compared to metal nanoparticles, oxide nanoparticles are perhaps more complex due to the presence of oxygen, hydroxyl, and aquo surface functional groups that lead to variation in particle stoichiometries.<sup>56</sup>

SO<sub>2</sub>(g) adsorption and transformation on mineral surfaces is a function of the mineral hydroxylation and hydration state, surface acidity and basicity, and surface structure (e.g., density of defect sites).<sup>16</sup> Goodman et al.<sup>45</sup> studied the interaction of SO<sub>2</sub>(g) with hydroxylated  $\alpha$ -Al<sub>2</sub>O<sub>3</sub> particle surfaces in the pressure range of 3–353 mTorr at 296 K. They proposed that strongly chemisorbed sulfite and bisulfite formed when SO<sub>2</sub>(g) reacted with basic surface groups (O<sup>2-</sup> and OH<sup>-</sup>). Matsumoto and Kaneko<sup>17</sup> studied SO<sub>2</sub>(g) adsorption on  $\gamma$ -FeOOH particles of various sizes (2–15 nm) and found that the amount of irreversible adsorption was weakly dependent on particle size and that SO<sub>3</sub><sup>2-</sup> and SO<sub>4</sub><sup>2-</sup> species were the primary surface products.

These prior studies of SO<sub>2</sub>(g) adsorption on metal oxide surfaces are qualitatively consistent with our results for the SO<sub>2</sub>(g)/ferrihydrite nanoparticle system, although we show that the chemistry is a function of particle size. On the basis of the frequency calculations and IR experimental measurements, the predominant surface species on the ferrihydrite nanoparticles was SO<sub>3</sub><sup>2-</sup>, with a minor concentration of SO<sub>4</sub><sup>2-</sup>. Assigning the majority of vibrational bands to SO<sub>3</sub><sup>2-</sup> was consistent with the absence of an oxidizing agent able to facilitate the conversion of SO<sub>2</sub> to SO<sub>4</sub><sup>2-</sup>. At present, there is no precedent to support a conceptual framework that would include the oxidation of SO<sub>2</sub> to SO<sub>4</sub><sup>2-</sup> with the concomitant reduction of Fe(III) to Fe(II) on ferric-bearing oxide surfaces. Other reducible metal oxides, however, such as Mn<sub>2</sub>O<sub>3</sub> and MnO<sub>2</sub>,<sup>57</sup> SnO<sub>2</sub>,<sup>58</sup> and CeO<sub>2</sub>,<sup>59</sup> have been observed to generate SO<sub>4</sub><sup>2-</sup> when interacting only with SO<sub>2</sub>(g). We postulate instead that SO<sub>3</sub><sup>2-</sup> was the dominant surface species resulting from the reaction of SO<sub>2</sub>(g) with the ferrihydrite nanoparticles. While a mechanism for this reaction remains elusive, it is likely that SO<sub>3</sub><sup>2-</sup> results from the reaction of SO<sub>2</sub>(g) with either surface water or hydroxyl groups associated with the adsorbing ferrihydrite nanoparticle:



With regard to the SO<sub>3</sub><sup>2-</sup> species, frequency calculations suggest the existence of monodentate and bidentate bridging coordination geometries, presumably with the sulfite oxygen bound to a metal cation site.

The IR measurements suggested that the adsorption and reaction of SO<sub>2</sub>(g) on ferrihydrite was sensitive to the nanoparticle size. After 1 h SO<sub>2</sub>(g) exposure time, the IR spectra showed that

(48) Cowley, J. M.; Janney, D. E.; Gerkin, R. C.; Buseck, P. R. *J. Struct. Biol.* **2000**, *131*, 210.

(49) Schwertmann, U.; Friedl, J.; Stanjek, H. *J. Colloid Interface Sci.* **1999**, *209*, 215.

(50) Chasteen, N. D.; Harrison, P. M. *J. Struct. Biol.* **1999**, *126*, 182.

(51) Munro, H. N.; Linder, M. C. *Physiol. Rev.* **1978**, *58*, 317.

(52) Henrich, V. E.; Cox, P. A. *The Surface Science of Metal Oxides*. Cambridge University Press: Cambridge, U.K., 1994.

(53) Preisinger, M.; Krispin, M.; Rudolf, T.; Horn, S.; Strongin, D. R. *Phys. Rev. B* **2005**, *71*, 165409.

(54) Lemire, C.; Meyer, R.; Shaikhutdinov, S. K.; Freund, H.-J. *Surf. Sci.* **2004**, *552*, 27.

(55) Lemire, C.; Meyer, R.; Shaikhutdinov, S. K.; Freund, H.-J. *Angew. Chem., Int. Ed.* **2004**, *43*, 118.

(56) Wachs, I. E. *Catal. Today* **2005**, *100*, 79.

(57) Kijlstra, W. S.; Biervliet, M.; Poels, E. K.; Bliet, A. *Appl. Catal. B* **1998**, *16*, 327.

(58) Gergely, B.; Guimon, C.; Gervasini, A.; Auroux, A. *Surf. Interface Anal.* **2000**, *30*, 61.

(59) Smirnov, M. Y.; Kalinkin, A. V.; Pashin, A. V.; Sorokin, A. M.; Noskov, A. S.; Bukhtiyarov, V. I.; Kharas, K. C.; Rodkin, M. A. *Kinet. Catal.* **2003**, *44*, 629.

the ratio of chemisorbed  $\text{SO}_2$  to sulfur oxyanion products was lowest on the 6 nm particle, implying that the larger particles led to the most rapid conversion of  $\text{SO}_2$  to  $\text{SO}_3^{2-}$ . This trend continued throughout the time of the experiment. After 20 h,  $\sim 50\%$  of the initial chemisorbed  $\text{SO}_2$  ( $1330\text{ cm}^{-1}$  mode) had been consumed on the 6 nm particle, in contrast to  $\text{SO}_2$  on the 3 nm ferritin-derived and reference ferrihydrite particles where there was only  $\sim 10\%$  loss in  $\text{SO}_2$ , relative to the initial  $\text{SO}_2$  concentration. Losses in  $\text{SO}_2$  were reflected in concomitant gains in the sulfur oxyanion surface species.  $\text{SO}_3^{2-}$  formation could be approximately quantified by analyzing the changes in the  $1330$  and  $1005\text{ cm}^{-1}$  vibrational bands, shown in Figure 7, that are assigned to chemisorbed  $\text{SO}_2$  and  $\text{SO}_3^{2-}$  species, respectively (for these purposes, any of the high-intensity vibrational modes between  $900$  and  $1050\text{ cm}^{-1}$  could have been chosen). For example, after 20 h the normalized FTIR intensity ( $I$ ) ratio for sulfite,  $I_{1005}/I_{1330}$ , was  $4.7 \pm 1$  for the 6 nm ferrihydrite particles, while it was  $1.1 \pm 0.5$  for the 3 nm and reference ferrihydrite particles. This simple analysis shows that the loss in chemisorbed  $\text{SO}_2$  is reflected in a gain of sulfite product and that the amount of this conversion was greatest for the larger 6 nm particle. After 60 h, chemisorbed  $\text{SO}_2$  was nearly exhausted on the 6 nm particles. In contrast, there was experimentally observable chemisorbed  $\text{SO}_2$  on the 3 nm particles after 60 h. Furthermore, the experimental observations and our associated interpretations suggest that the ferritin-derived 2-line ferrihydrite ( $\sim 3$  nm particle) and reference 2-line material synthesized by standard solution chemistry exhibited similar chemistry. This similarity is consistent with a unique electronic or structural property that is associated with the smaller 3 nm particle. In other words, the 3 nm particle reactivity was independent of the synthetic route used for its manufacture. A remaining question is what property of the 3 nm particles alters their reactivity compared with that of the 6 nm particles.

STS and TEM measurements suggested that there were structural differences between the 3 and 6 nm particles. Measurement of the band gap corresponding to the smaller particles ( $1.5\text{ eV}$ ) was significantly lower compared with the larger particles ( $2.5\text{ eV}$ ), the latter being similar to what would be expected for bulk iron oxyhydroxide. TEM showed that the smaller particles were much less crystalline (relatively amorphous). These experimental observations may be consistent with the smaller particles having more surface defects compared with the larger particles. Prior work has suggested this to be the case when the difference of surface energy as a function of size is considered for nanoparticles.<sup>60</sup> In general, however, the larger particles showed a more complete conversion of  $\text{SO}_2(\text{g})$  to  $\text{SO}_3^{2-}$ . An increased availability of structural (or adsorbed) water on the larger ferrihydrite particles may be one reason for the more complete conversion (see reaction 1 above). This possibility is offered with some caution, since recent ongoing synchrotron-based X-ray scattering research on inorganically synthesized ferrihydrite (non-ferritin-based particles) suggests that the smaller 3 nm particles have more water associated with them than their

larger and more crystalline 6 nm counterparts.<sup>22</sup> Hence, if the reaction of water with  $\text{SO}_2$  is a key reaction step in the production of  $\text{SO}_3^{2-}$ , then the specifics of how water is bonded in the different size particles may be more important than the total water content. Prior work<sup>45</sup> on less hydrous oxide surfaces, however, that has investigated the conversion of  $\text{SO}_2(\text{g})$  to  $\text{SO}_3^{2-}$  has implicated the role of lattice  $\text{O}^{2-}$  and/or  $\text{OH}^-$ . Differences in the energetics involved in the reaction between  $\text{SO}_2$  and lattice oxygen associated with the different nanoparticles may also be a factor in determining the production of sulfite. While our experiments do not allow us to precisely explain the observation of slower conversion of  $\text{SO}_2(\text{g})$  to  $\text{SO}_3^{2-}$  on the 3 nm particles, the experimental observations do show that the reaction of  $\text{SO}_2(\text{g})$  with ferrihydrite was sensitive to the particle size (directly or indirectly). Future experiments in our laboratory investigating the structure of ferrihydrite (synthesized by both inorganic and biomimetic means) as a function of size should help better describe any surface reactions on this environmentally ubiquitous material.

## 5. Summary

Ferrihydrite nanoparticles with nominal sizes of 3 and 6 nm were synthesized by use of ferritin, with loadings of 500 and 2000 Fe atoms/protein, respectively. The protein shell surrounding ferrihydrite was subsequently removed at a temperature of 373 K. These protein-free nanoparticles were compared to synthetic 2-line ferrihydrite nanoparticles prepared by traditional non-biomimetic techniques. HRTEM analysis showed that the 6 nm ferritin-derived particles were significantly more crystalline than the 3 nm particles. The 6 nm ferritin-derived particle structure was consistent with 6-line ferrihydrite, while the 3 nm ferritin-derived particles were consistent with 2-line ferrihydrite. STS analysis showed that the band gap of the ferrihydrite nanoparticles was a function of their size. Larger particles exhibited a band gap consistent with bulk iron oxides, while the smaller particles had a smaller band gap, presumably attributed to a high surface defect density. Adsorption and reaction of  $\text{SO}_2(\text{g})$  on each of the ferrihydrite nanoparticles led primarily to the formation of sulfite (with small contributions possibly arising from sulfate). The amount of  $\text{SO}_2(\text{g})$  converted to sulfite complexes was greatest on the 6 nm particles. The 3 nm ferritin-derived and reference ferrihydrite particles showed similar but slower conversion of  $\text{SO}_2(\text{g})$  than was associated with the 6 nm particles.

**Acknowledgment.** D.R.S. acknowledges the partial support of this research by the Center for Environmental Molecular Science (CEMS) at Stony Brook (NSF-CHE-0221934), U.S. Environmental Protection Agency (EPA), and the donors of the Petroleum Research Fund (PRF), administered by the American Chemical Society. High-energy XRD measurements were performed at X-ray Operation and Research (XOR) beamline 11-IDB at the Advanced Photon Source, Argonne National Laboratory. Use of the APS is supported by the U. S. Department of Energy (DOE), Office of Science, Office of Basic Energy Sciences, under Contract No. W-31-109-Eng-38.

LA0602214

(60) Banfield, J. F.; Zhang, H. *Nanoparticles in the environment*; The Mineralogical Society of America: Washington, DC, 2001; Vol. 44, pp 1–58.